Probing the mechanisms of morphological evolution and phase selection of intermetallic compounds for impurity-tolerant processing of recycled Al alloys

Shikang Feng*[a,b], Mika Shearwood[c], Andrew Lui[a], Dominic Banks[c], Tim Nicholls[c], Sion Richards[c], Matthew D. Wilson[c], Patrick S. Grant[a], and Enzo Liotti[a]

[a] *Department of Materials, University of Oxford, Oxford, OX1 3PH, UK*
[b] *School of Engineering and Informatics, University of Sussex, Brighton, BN1 9RH, UK*
[c] *Science and Technology Facilities Council, Rutherford Appleton Laboratory, Harwell Science and Innovation Campus, Didcot, OX11 0DE, UK*

Abstract

Fe-rich intermetallic compounds (IMCs) are a persistent challenge in the recirculation of secondary aluminium alloys. Despite significant research effort, largely via post-solidification studies, the mechanisms governing IMC phase selection in higher-Fe (>1 wt.%), recycled Al alloys and how they can be controlled to facilitate more benign IMC species and/or morphologies remain poorly understood. This creates barriers to compositional and process design for more Fe-tolerant alloys. In this paper, we present a systematic real-time investigation of IMC formation, phase selection and morphological evolution in recycled 3xx series Al alloys with elevated Fe concentrations (up to 2.5 wt.%), using *in situ* synchrotron X-ray radiography. Coupled with thermodynamic simulations, we develop a method to reliably estimate the formation temperatures of primary α-AlFeSi and β-AlFeSi IMCs, and show direct insights into their formation sequence and kinetics. Contrary to widely held assumptions based on low Fe-containing (<0.6 wt.%) primary alloys, we show that in recycled alloys containing higher Fe concentrations, increased cooling rate significantly promotes the formation of the more anisotropic β-AlFeSi (over the more compact α-AlFeSi), which however can be fully suppressed at slow cooling. We propose how a solute-suppression mechanism kinetically controls the α/β IMC phase evolution. Further, we reveal and quantify a faceted-to-non-faceted morphological transition of α-AlFeSi from a faceted polyhedral to non-faceted near-equiaxed dendritic morphology. This transition is governed by an interplay between solidification velocity and liquid undercooling at the local IMC/liquid interfaces. This study provides insights into how solidification conditions may be leveraged to improve microstructural control in high Fe-containing recycled alloys.

*Corresponding author.
Email addresses: shikang.feng@materials.ox.ac.uk; shikang.feng@sussex.ac.uk (S. Feng).

Keywords: *Al recycling; Intermetallic compounds (IMCs); Faceted-to-non-faceted transition; Phase selection; Solute suppression*

1 Introduction

The required global transition towards more sustainable metal production has placed unprecedented importance on metal recycling. Amongst aluminium systems, Al-Si based alloys, widely used in automotive, aerospace and construction sectors attract particular interest for recycling due to their widespread availability, for example in end-of-life internal combustion engine blocks. However, the increased Fe content commonly introduced through recycled scrap significantly compromises alloy mechanical performance by promoting the formation of coarse (typically in the range of ∼30 µm to several millimetres [1]), brittle Fe-rich intermetallic compounds (IMCs). Over the past few decades, a large number of Fe-rich IMCs have been reported in various types of Al alloys [2–16], and in Al-Si systems the most commonly observed IMCs include α-$Al_{15}(Fe,Mn)_3Si_2$ (α-AlFeSi), β-Al_5FeSi (β-AlFeSi) and θ-$Al_{13}Fe_4$. These IMCs, such as the monoclinic plate-like β-AlFeSi, can serve as crack initiation sites, and degrade tensile ductility and fatigue life [17–19]. A major scientific and technological challenge in aluminium recycling is therefore to control the type, size, morphology, and distribution of Fe-rich IMCs during solidification. Addressing this challenge is key to the development Fe-tolerant alloys with benign microstructure and preserved performance.

Strategies to mitigate the adverse effects of Fe during primary alloy fabrication have relied on minor additions of neutralising elements (e.g. Mn, Cr and Co) to stablise the more compact, cubic α-AlFeSi IMCs over the more deleterious, plate-like β-AlFeSi [20–34]. Furthermore, a number of studies suggested that increasing cooling rate can kinetically suppress β-IMC formation, in favour of the more benign α-AlFeSi phases [35–38]. However, these findings are predominantly based on relatively low Fe-containing (<0.6 wt.%) commercial alloy systems, and the underlying mechanisms governing phase selection in higher Fe-containing (>1 wt.%) recycled alloys remain unclear. Moreover, the analysis of

IMC phase evolution has been constrained by reliance on post-solidification studies (e.g. electron microscopy), which provide little insight into the dynamic interplay between solidification conditions, solute segregation, and phase formation. Although thermal analysis, such as differential scanning calorimetry (DSC), has been widely used to analyse phase transformations during alloy solidification, it is limited to low cooling rates (below $1\,\mathrm{K\,s^{-1}}$) [39–41]. Further, DSC relies on detecting enthalpy changes associated with phase transformations within the entire sample. This poses challenges to the accurate detection of minority IMC formation when the first IMC crystal starts to form from the liquid.

With the development of ever more capable *in situ* X-ray imaging techniques, increasing effort has been spent on understanding solidification kinetics in higher Fe-containing (>1 wt.%) Al alloys, both driven by the urgent need of alloy recycling and the advantage of better X-ray absorption imaging contrast. To date, *in situ* studies of Fe-rich IMCs have focused on crystal formation and growth, mostly in simple model alloy systems, such as hypereutectic Al-Fe [39, 42–49]. Insights gained include crystal nucleation bursts during early-stage IMC formation [46], IMC refinement via inoculant additions [44, 45] and anisotropic lateral growth via a twin plane re-entrant (TPRE) mechanism [43, 47]. Most recently, studies demonstrated that applying external fields at the right stage of solidification can lead to refinement of Fe-rich IMCs [49]. However, so far there is limited understanding of the kinetics of IMC phase evolutions in compositionally complex, recycled alloys, and it is not clear how IMC phase species and morphologies can be controlled by manipulating solidification parameters to facilitate more Fe-tolerant microstructure.

In this study, we present a systematic real-time investigation into the phase selection and morphological evolution of critical Fe-rich IMCs during solidification of recycled 3xx Al alloys with elevated Fe concentrations (up to 2.5 wt.%). Using *in situ* synchrotron X-ray radiography coupled with thermodynamic simulations, we develop a method to reliably estimate the formation temperatures of individual IMC phases as they start to form from liquid. This allows solidification sequences and complex IMC phase evolutions under different cooling conditions to be clearly unveiled. Contrary to earlier assumptions based

on lower-Fe (<0.6 wt.%) primary alloys, we show that in highly Fe-contaminated (2.5 wt.%) alloys, increasing cooling rate facilitates the formation of the more anisotropic β-AlFeSi (over α-AlFeSi) whilst lower cooling rates suppress it — a reversal of the behaviour commonly reported in lower-Fe systems.

We suggest a mechanistic explanation for the phase selection between α- and β-AlFeSi IMCs, accounting for solute segregation (depletion) in the liquid, evolution of liquid undercooling, and competition between the growth of pre-existing, higher-temperature α-AlFeSi and the nucleation of subsequent, lower-temperature β-AlFeSi. Furthermore, we uncover, in real time, a faceted-to-non-faceted morphological transition of α-AlFeSi crystals from polyhedron to near-equiaxed dendrites. We show that this transition is governed by an interplay between solidification velocity and the local liquid undercooling at the growing IMC/liquid interfaces. These findings support predictions by Jackson's surface roughness model [50, 51], and provide a basis for IMC morphological control. Finally, we map our findings onto a continuous cooling transformation (CCT) framework, offering practical guidance for alloy designers and casting engineers.

2 Experimental Methods

2.1 Alloy preparation

A commercial 3xx cast Al alloy, supplied by Rio Tinto, was employed as the base alloy. Additional Fe was then added to obtain total Fe concetrations of 1.2wt.% and 2.5wt.% respectively, simulating Fe-contaminated recycled alloys. The two alloys are thereby named 1.2Fe and 2.5Fe, respectively. The alloy of each Fe concentration was prepared in the following procedure. First the base 3xx alloy was fully melted in an induction furnace with Ar gas shielding, and an Al-80Fe (wt.%) master alloy were added to the melt. The alloy melt was held at 850 $\pm$ 3°C for 40 minutes, with electromagnetic stirring and careful mechanical stirring to promote mixing. The melt was then cast into an ASTM standard Type B steel mould (ASTM International designation: E716 [52]), preheated at 150 °C.

This mould is known to promote freezing at a cooling rate of $\sim$50 K s^{-1} that prevents any significant macro-segregation [52]. The outcome was a disk ingot of $\sim$55 mm diameter and $\sim$10 mm thickness, as shown schematically in Fig. S1 in the supplementary materials (SM). The final alloy compositions were measured by optical emission spectroscopy and are given in Table 1.

Table 1: Composition of alloys 1.2Fe and 2.5Fe determined by optical emission spectroscopy. Any unlisted elements were present at <0.01wt.%.

Sample	**Composition (wt.%)**						
	Si	Fe	Mg	Mn	Ti	Sr	Al
1.2Fe	10.13	1.23	0.31	0.39	0.04	0.01	Balance
2.5Fe	9.97	2.54	0.30	0.38	0.04	0.01	Balance

2.2 Synchrotron sample preparation

Foil samples for X-ray radiography were sliced from the ingot (Fig. S1) using wire electro-discharge machining (wire EDM). Then samples of 20×10 mm and thickness of 200 ± 5 µm were prepared by grinding and polishing to a final surface finish of 1 µm. Each sample was encapsulated in an X-ray transparent BN cell (Multi-lab, UK) of 100 µm thickness.

2.3 Synchrotron X-ray radiography

In situ synchrotron X-ray radiography experiments were carried out at beamline I13-2, Diamond Light Source (DLS), UK, using a bespoke solidification rig that has been described elsewhere [43, 44, 46, 48, 53, 54]. The rig was operated with a controlled Ar atmosphere to protect foil alloy samples and heating elements from oxidation. During solidification experiments, foil samples were illuminated with a pink X-ray beam peaking at an energy of 25 keV. The transmitted beam through the sample was collected onto a GAGG:Ce single crystal scintillator, which then projected the image onto a Hamamatsu ORCA-Quest CMOS detector through a 4× objective lens system. Radiography videos were recorded at 10 Hz with an image pixel size of 1.15 μm/pixel.

Each sample was fully melted and held at 720°C for 3 min, then cooled under isothermal cooling, at constant cooling rates ranging from 0.5 Ks^{-1} to 8 Ks^{-1}. Table 2 lists the alloy samples and all the experimental conditions, together with the number of repeats in each condition. Overall, 35 experiments were carried out. Details of synchrotron image processing are provided in section S2 in the SM.

Table 2: Summary of alloy samples and experimental conditions, showing the number of repeats in each condition.

Alloy	**Cooling rate (Ks^{-1})**			
	0.5	2	4	8
1.2Fe	4	5	5	4
2.5Fe	4	4	5	4

2.4 Estimation of IMC start temperature

Feng *et al.* [42] developed a method of estimating the growth temperatures of secondary IMCs by using a well-defined solidification front with well-known equilibrium temperature as an *in situ* temperature reference. A similar method was developed here to allow estimation of the formation start temperatures of different primary Fe-rich IMC phases during the solidification of multi-element recycled alloys, in this case by using eutectics as temperature references.

Fig. 1(a) shows a pseudo-binary phase diagram of Al-10Si-0.3Mg-0.5Mn as a function of Fe concentration, computed with FactSage 8.2 using the FTlite database. The alloy Fe concentrations studied in this work are indicated by red dashed lines in Fig. 1(a), with Figs. 1(b) and (c) showing the mass percentage of phases as a function of temperature for 1.2Fe and 2.5Fe, respectively. Alloy 1.2Fe has a solidification range from 615 °C to 565 °C (alloy solidus), and alloy 2.5Fe has a solidification range from 645 °C to 565 °C. For clarity, Table 3 lists the equilibrium start temperatures of solid phases of the two alloys. Alloy 1.2Fe forms α-AlFeSi (α-IMC) as the only primary IMC, with an equilibrium start temperature of 615 °C. At a higher Fe concentration, alloy 2.5Fe forms two primary

IMCs, i.e. α-AlFeSi (α-IMC) and β-AlFeSi (β-IMC), with equilibrium start temperatures of 645 °C and 634 °C.

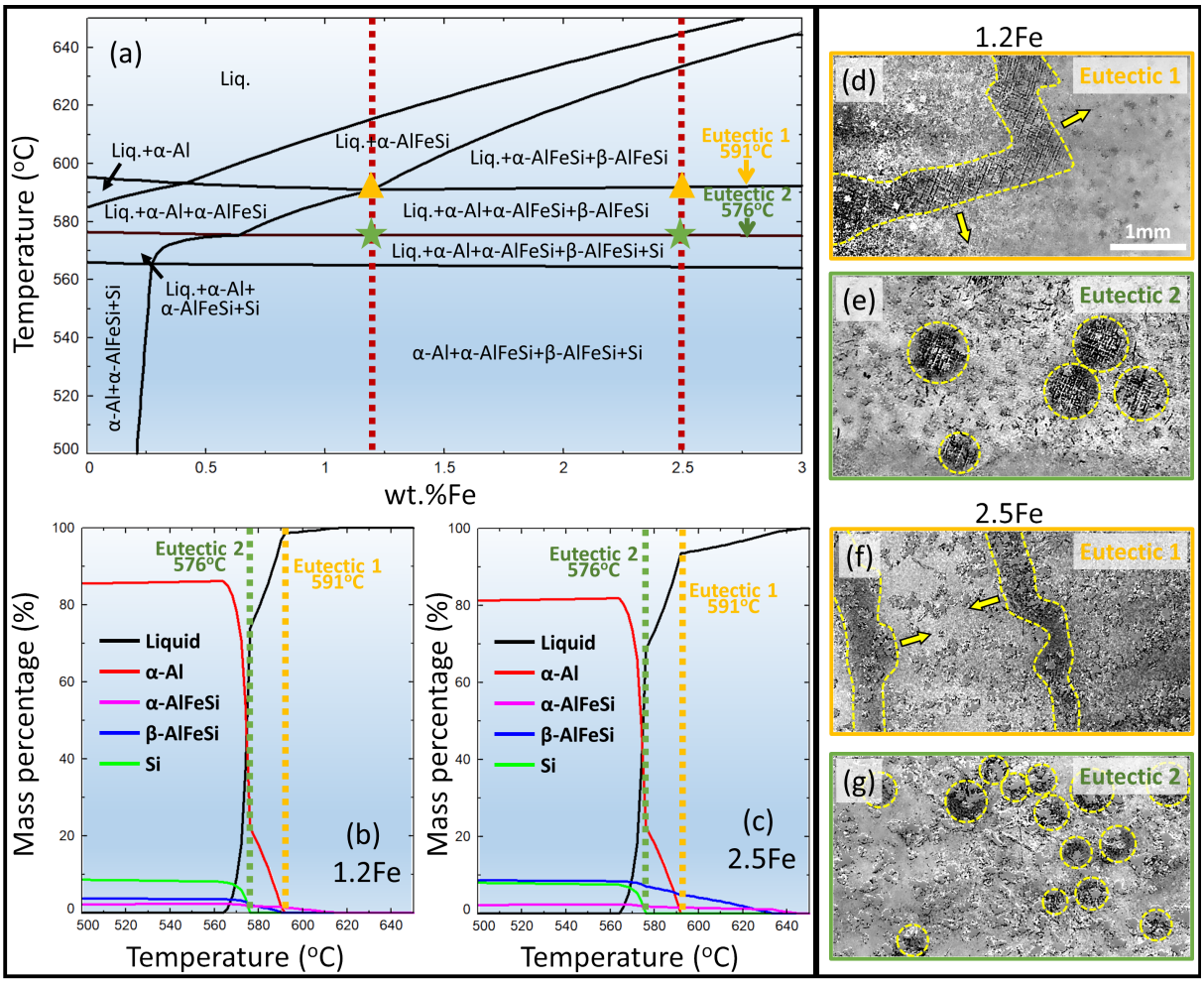

Figure 1: (a) A pseudo-binary phase diagram of Al-10Si-0.3Mg-0.5Mn as a function of Fe concentration. The orange and green arrows indicate the start temperatures of the two eutectics in the system. (b and c) Mass percentage of phases as a function of temperature for (b) 1.2Fe and (c) 2.5Fe, respectively. In each case, the start temperatures of the eutectics are labelled and marked by dashed lines. (d and e) Radiographic images (each subtracted from the image 10 frames before it) of the two eutectics in alloy 1.2Fe, which is darker in contrast (as highlighted by dashed yellow curves/circles). (f and g) Radiographic images (each subtracted from the image 10 frames before it) of the two eutectics in alloy 2.5Fe.

Noticing that the start temperatures of eutectics 1 and 2 remained constant across the Fe concentration range studied, the two eutectics were employed respectively as *in situ* temperature references for estimation of IMC formation start temperatures. The radiographic images in Figs. 1(d) to (g) (each subtracted from the image 10 frames before it) show two eutectics in both alloys, appearing darker in contrast (as highlighted by dashed yellow curves/circles). It is worth noting that in each case, the eutectic did

Table 3: Equilibrium start temperatures of solid phases in alloys 1.2Fe and 2.5Fe, obtained from Figs. 1(b) and (c).

Phase	**Equilibrium start temperature (°C)**	
	1.2Fe	2.5Fe
Primary α-IMC	615	645
Primary β-IMC	-	634
Eutectic 1 (α-Al+β-IMC)	591	591
Eutectic 2 (α-Al+β-IMC+Si)	576	576

not propagate unidirectionally with a single front, but appeared relatively randomly (and simultaneously) across the field of view and grew to merge with one another as solidification proceeded. This indicated good isothermal cooling conditions, as intended. Using the appearance of each eutectic as a known temperature reference, the start temperatures for the formation of primary Fe-rich IMC phases were obtained by calculating the time difference Δt between the first appearance of the IMCs and the eutectic, and multiplying with the constant, accurately controlled cooling rate $\dot{T}$, i.e. $T_{IMC} = T_{Eut} + \Delta t \cdot \dot{T}$. The maximum deviation in the IMC start temperatures obtained using the two eutectic temperature references was $\pm 0.5\,^{\circ}\mathrm{C}$.

2.5 Tracking of IMC growth

To track and measure the growth velocities of primary IMC crystals, a frame-by-frame interface tracking approach was employed using optical flow analysis. Specifically, a built-in implementation of the Farneback optical flow algorithm [55] in MATLAB was used to estimate the pixel-wise velocity field between consecutive radiographic frames. Since each IMC crystal remained stationary after nucleation, the algorithm tracked accurately the propagation of IMC/liquid interfaces over time. For each IMC, the normal component of the interface velocity to the growing interface was then extracted as a function of time after formation.

3 Results

Fig. 2 shows radiographic image sequences from the solidification of alloy 1.2Fe at (a) $0.5\,\mathrm{K\,s^{-1}}$, (b) $2\,\mathrm{K\,s^{-1}}$, and (c) $8\,\mathrm{K\,s^{-1}}$ under isothermal cooling conditions. At each cooling rate, the formation of primary α-IMCs, with a faceted, polyhedral morphology, occurred randomly (spatially) within the field of view. The primary IMCs very likely formed preferentially on sample oxide walls as there was no intentional addition of inoculants (or refiners), and IMCs remained spatially anchored. An example of faceted α-IMCs that formed on wall oxides can be seen in the inset image in Fig. 2(a). As the cooling rate increased from $0.5\,\mathrm{K\,s^{-1}}$ to $8\,\mathrm{K\,s^{-1}}$, the primary α-IMCs became increasingly finer, reducing in average size from 82±18µm to 21±9µm.

Fig. 3 shows radiographic image sequences for the solidification of the more concentrated 2.5Fe alloy under isothermal cooling conditions from $0.5\,\mathrm{K\,s^{-1}}$ to $8\,\mathrm{K\,s^{-1}}$. Similarly, all IMCs remained static after formation. However, different from the 1.2Fe alloy, the 2.5Fe alloy involved more complex phase and IMC morphological evolutions as a function of cooling rate. First, at the lowest cooling rate of $0.5\,\mathrm{K\,s^{-1}}$ (Fig. 3(a)), only α-IMCs formed as the primary phase, and there were no subsequent primary β-IMCs. This differed from the thermodynamic prediction (Fig. 1(c)), meaning that primary β-IMC formation was suppressed. Then, increasing the cooling rate to $2\,\mathrm{K\,s^{-1}}$ led to an increasing number of α-IMCs and the formation of two primary, plate-like β-IMCs in the field of view (FoV) towards the later stage of solidification (as highlighted by the yellow ellipse in Fig. 3(b)). Further increase in cooling rate led to reduced primary α-IMC formation and significantly increased primary β-IMC formation (Fig. 3(c)). Eventually primary β-IMCs became dominant at $8\,\mathrm{K\,s^{-1}}$ (Fig. 3(d)). Overall, 86 α-IMCs formed at $0.5\,\mathrm{K\,s^{-1}}$, 218 α-IMCs at $2\,\mathrm{K\,s^{-1}}$, 157 α-IMCs at $4\,\mathrm{K\,s^{-1}}$, and 81 at $8\,\mathrm{K\,s^{-1}}$.

To study the microstructure at higher cooling rates beyond those achievable in the furnace designed for the *in situ* synchrotron experiments, a rod sample (8 mm diameter) of the 2.5Fe alloy was cast in a water-cooled copper mould (cooling rate $\sim 100\,\mathrm{K\,s^{-1}}$). Post-solidification electron backscattered imaging showed that β-IMCs were the predominant

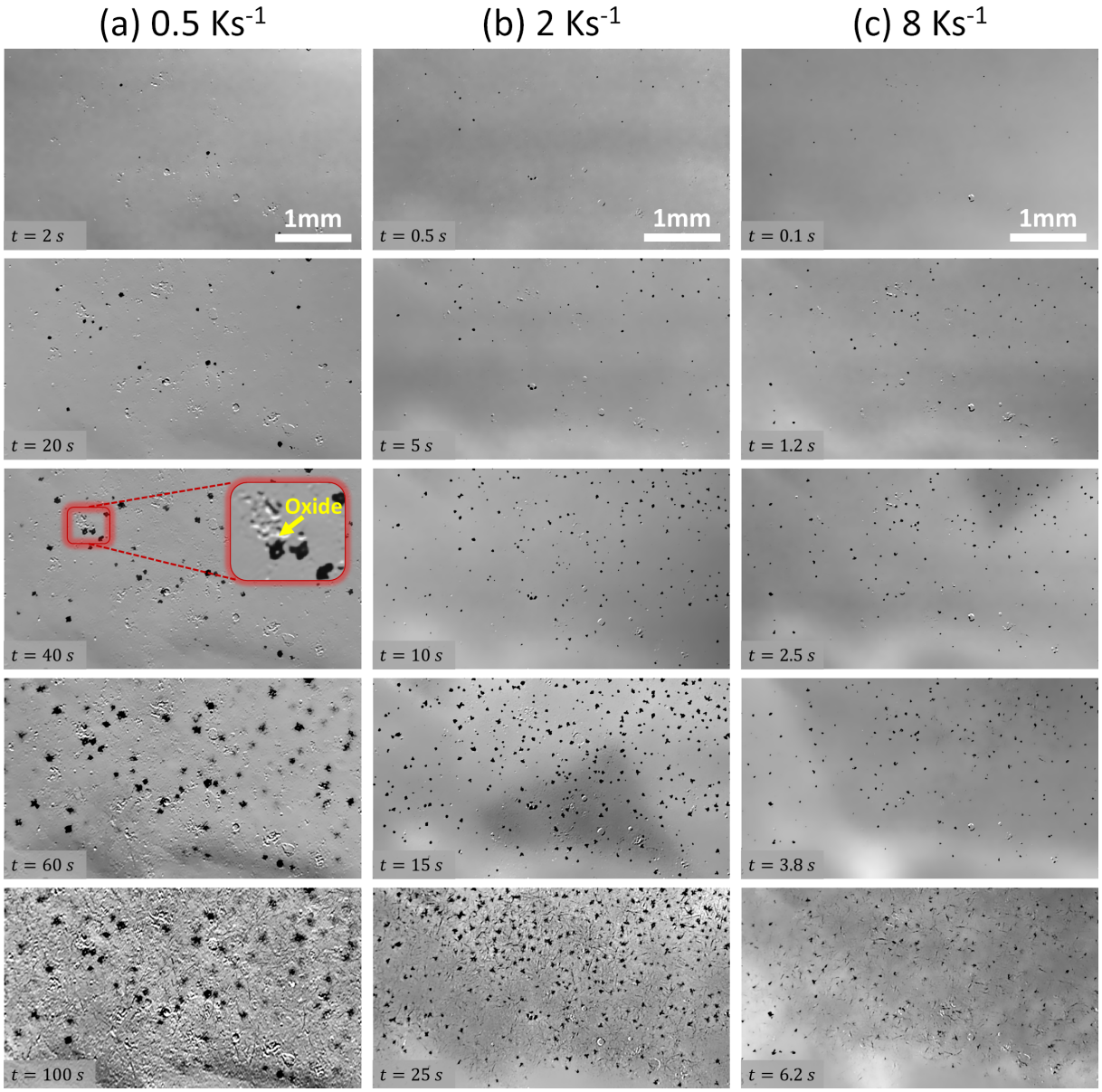

Figure 2: Radiography sequences showing the formation of primary α-IMC during isothermal solidification of alloy 1.2Fe at (a) $0.5\,\mathrm{K\,s^{-1}}$, (b) $2\,\mathrm{K\,s^{-1}}$, and (c) $8\,\mathrm{K\,s^{-1}}$. Time $t = 0$ was set when an IMC crystal first appeared in the field of view.

IMC phase, with very few α-IMCs, as shown in Fig. S4 in the SM. This agrees well with the trend observed *in situ*. Contrary to the general understanding that higher cooling rates should favour α-IMCs and suppress the more anisotropic β-IMCs [1, 38, 56, 57], this work showed that higher cooling rates promoted the formation of β-IMCs, for more Fe-contaminated alloys. It is also worth noting that previous studies were based on post-mortem microscopy of relatively large cast ingots (centimeter-scale or larger), where the actual local cooling conditions and segregation behaviour that dictated IMC formation

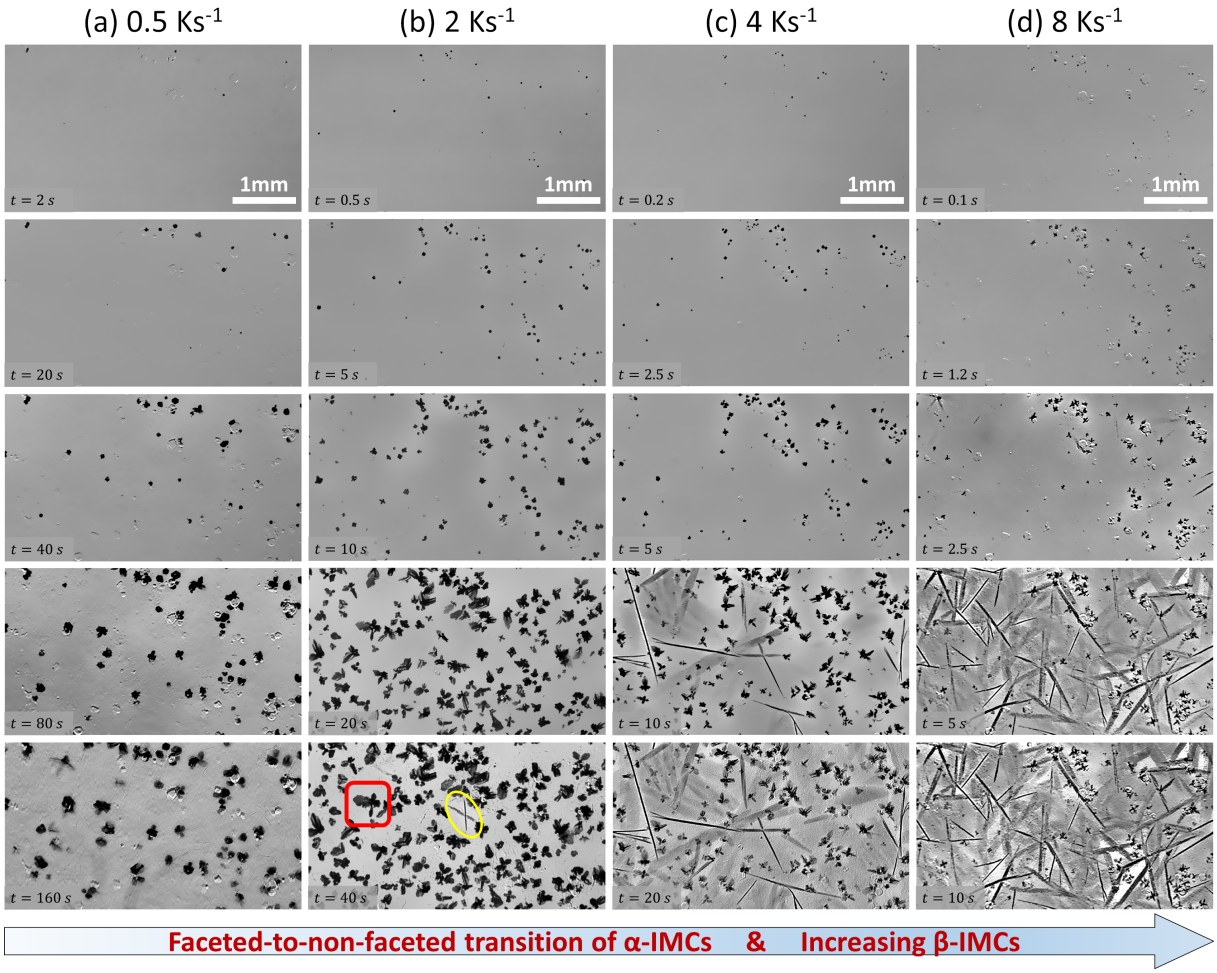

Figure 3: Radiography sequences showing the formation of primary α-IMC during isothermal solidification of alloy 2.5Fe at (a) $0.5\,\mathrm{K\,s^{-1}}$, (b) $2\,\mathrm{K\,s^{-1}}$, (c) $4\,\mathrm{K\,s^{-1}}$, and (d) $8\,\mathrm{K\,s^{-1}}$. Time $t = 0$ was set when an IMC crystal first appeared in the field of view.

might be difficult to know/control. The mechanism governing the IMC phase selection here, as a function of cooling rate, will be elaborated later.

In alloy 2.5Fe, not only did the cooling rate affect the phase selection between α- and β-IMCs, it also resulted in a clear morphological transition of the α-IMCs, from faceted, polyhedral at $0.5\,\mathrm{K\,s^{-1}}$, to non-faceted, dendritic at $2\,\mathrm{K\,s^{-1}}$ and above (Fig. 3). Compared with faceted crystal morphologies that have sharp, flat interfaces with the alloy matrix - known to be deleterious for load transfer and crack resistance - non-faceted morphologies are generally considered more benign for alloy processability and mechanical properties [58–60]. Fig. 4 shows the detailed growth sequence of a dendritic IMC at $2\,\mathrm{K\,s^{-1}}$ (highlighted by a red box in Fig. 3(b)). The instantaneous growth velocities since

first appearance were tracked using optical flow methods, and a colour map of velocity distribution (shown as quivers) is superimposed on each radiograph in Fig. 4. The IMC was initially near-circular (in 2D projection) (Fig. 4(a)), and with approximately isotropic growth velocity (Fig. 4(b)). Then, from $t = 7s$ onwards (Fig. 4(c)), the IMC started to show anisotropy in growth velocity and crystal morphology, and developed gradually into a dendritic morphology (Figs. 4(d), (e) and (f)). The inset image in Fig. 4(f) shows the development of secondary dendrite arms (highlighted by red arrows) in the later stages.

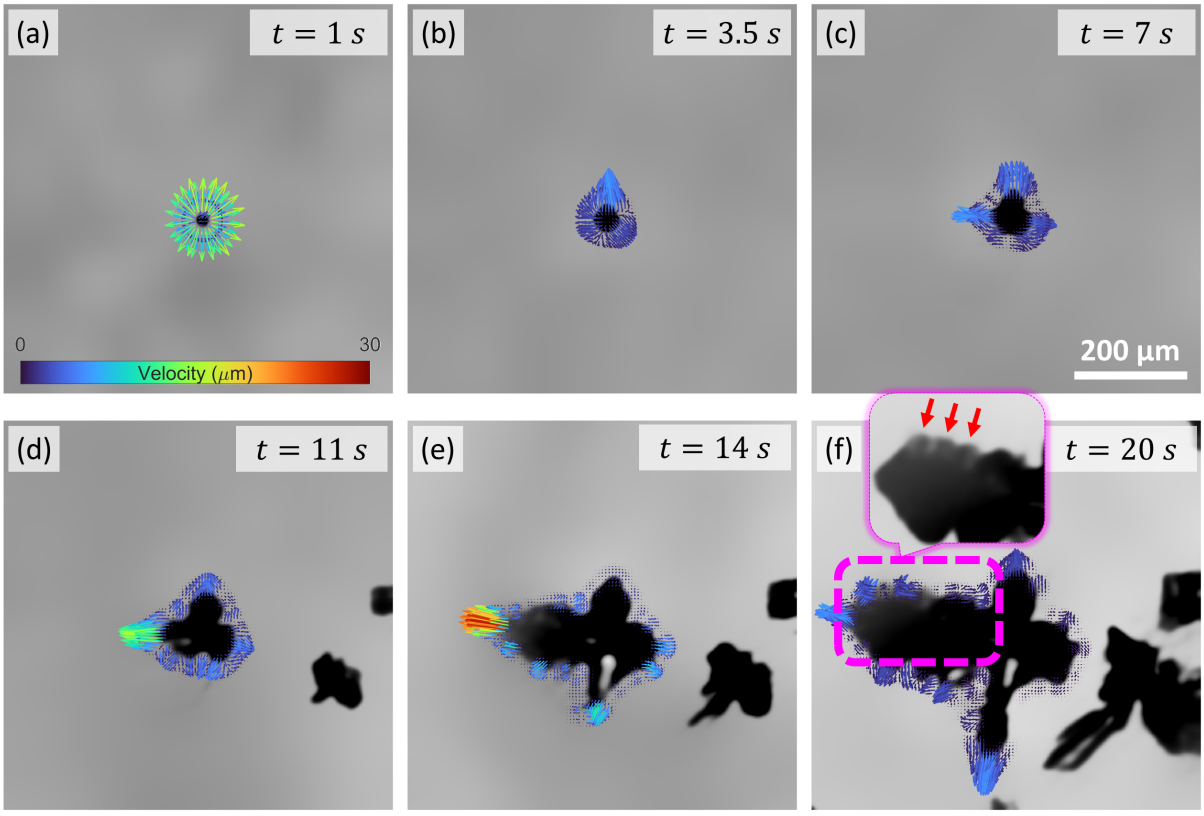

Figure 4: Radiography sequences superimposed with instantaneous growth velocity fields, showing the growth of a non-faceted, dendritic α-IMC in alloy 2.5Fe at $2\,\mathrm{K\,s^{-1}}$ (highlighted by a red box in Fig. 3(b)). The red arrows in the inset image of (f) highlight the secondary arms of the dendritic IMC.

To better understand this dendritic growth of α-IMCs, Fig. 5 shows the interface growth velocities (i.e. the local solid/liquid interface velocities) of the same α-IMC as a function of time, along the directions of D1 and D2 shown in the inset. Time $t = 0$ marked the first appearance of the crystal. The two velocity profiles followed the same trend and their evolutions were generally synchronised with respect to time. After transient growth with a peak velocity of $\sim$15 µm s^{-1} for the first 1 s (Fig. 4(a)), the velocity then reduced

and remained relatively steady until $t \approx 10$ s. Then there was a rapid surge in velocities along both directions, leading to a peak velocity of $\sim 40\,\mu\mathrm{m\,s^{-1}}$ between $t \approx 10$ s and $t \approx 15$ s (Fig. 5). Correspondingly, the dendrite arms appeared and developed rapidly during this period (Figs. 4(d) and (e)) .

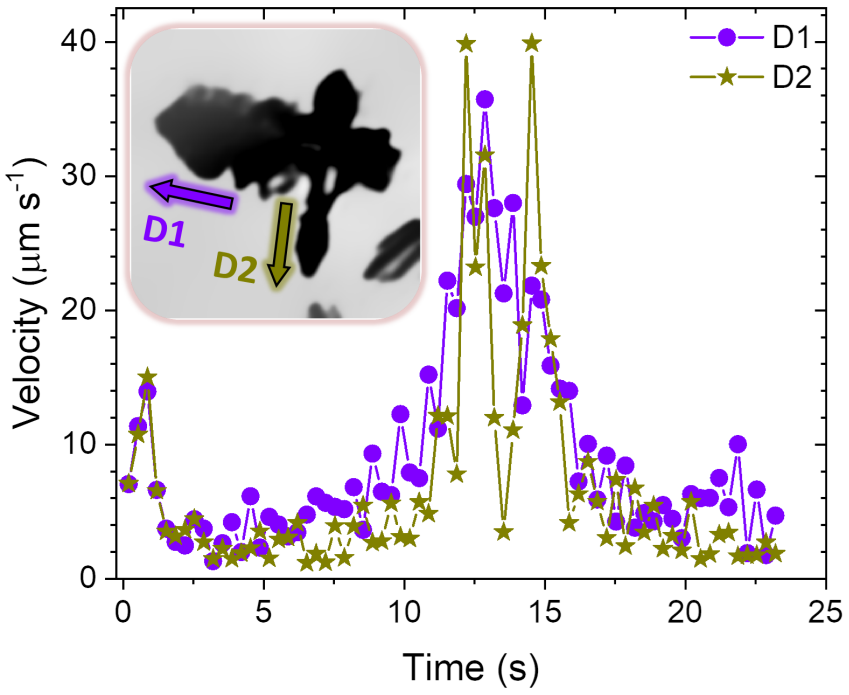

Figure 5: Growth velocities of the α-IMC in Fig. 4, along the directions of dendrite arms D1 and D2 (shown in the inset image).

In contrast to the non-faceted, dendritic α-IMCs, Fig. 6 shows the growth sequence for a faceted, polyhedral α-IMC, again superimposed with the instantaneous velocity map. The IMC adopted a similar, near-circular (in 2D) morphology at the early stage following its formation (Fig. 6(a)). Then, growth anisotropy started to resolve (from $t = 9$ s). However, compared with the dendritic IMC (Fig. 4), the magnitude of its growth velocities (i.e. the local solid/liquid interface velocities) were significantly lower. Local areas of the interface that experienced comparatively high velocity developed into sharp corners, and areas that remained quasi-static (i.e. local velocity ~ 0) became smooth facets. These *in situ* observations agree qualitatively with studies of crystal facets in solidifying transparent non-metallic alloy systems [61, 62]. According to the Wulff facets theorem [63] and the Burton–Cabrera–Frank (BCF) model [64], fast growing

planes (associated with higher surface energies) tend to diminish, leaving behind the slow growing planes as facets bounding the crystal, governed by the minimisation of total surface or interfacial energy. More time-resolved radiography sequences of dendritic and polyhedral α-IMC growth and post-solidification SEM images of the IMCs are provided in section S3 in the SM.

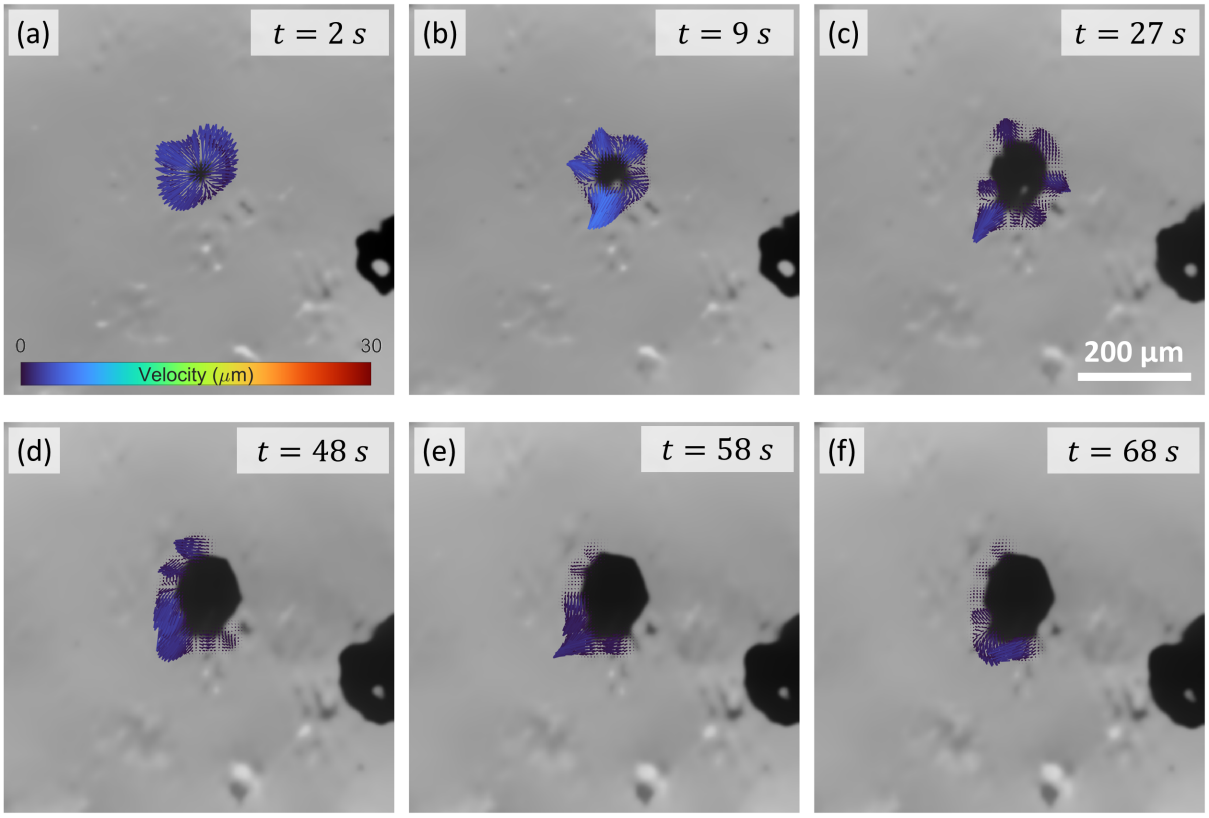

Figure 6: Radiography sequences superimposed with instantaneous interfacial growth velocity, showing the growth of a faceted, polyhedral α-IMC in alloy 2.5Fe at $0.5\,\mathrm{K\,s^{-1}}$.

Fig. 7 compares the maximum instantaneous IMC/liquid interface velocity for the non-faceted, dendritic α-IMC (Fig. 4) and the faceted, polyhedral α-IMC (Fig. 6). Overall, the polyhedral α-IMC grew steadily with a median velocity of $1.2\,\mu\mathrm{m\,s^{-1}}$, whereas the dendritic α-IMC grew with a median velocity of $8\,\mu\mathrm{m\,s^{-1}}$ and with a peak velocity of $40\,\mu\mathrm{m\,s^{-1}}$ during dendrite arm formation.

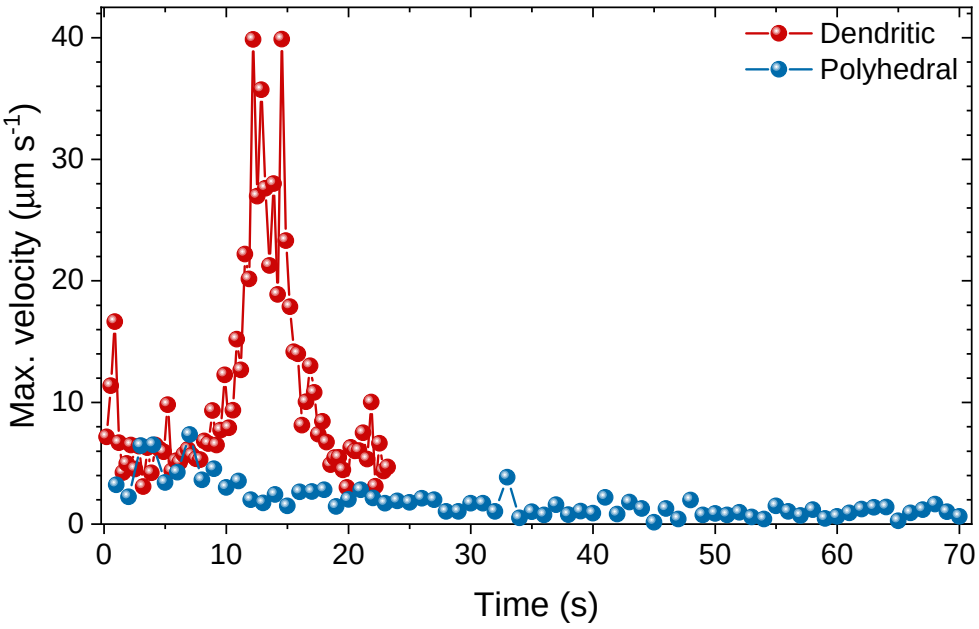

Figure 7: Maximum instantaneous growth velocities (i.e. solid/liquid interface velocities) for the non-faceted, dendritic α-IMC in Fig. 4 and the faceted, polyhedral α-IMC in Fig. 6, for alloy 2.5Fe.

4 Discussion

4.1 Morphological transition of α-IMC

One of the most widely accepted theories to describe faceted and non-faceted crystal growth is the interface morphology theory proposed by Jackson [50, 51], based on the concept of interface roughness and interfacial free energy minimisation. By assuming an initially atomically flat surface, the change in the surface free energy upon adding atoms to fill up a fraction f of N possible sites on a crystal plane at equilibrium temperature T_E is given by:

$$\frac{\Delta G}{NkT_E} = \alpha f(1-f) + flnf + (1-f)ln(1-f) \tag{1}$$

where $\alpha = \frac{\Delta S}{R}\xi$ is the Jackson factor, ΔS is the entropy of fusion, R is the gas constant, and ξ ($\xi < 1$) is a factor dependent on the crystallography of the interface. Fig. 8(a) plots the relative free energy $\frac{\Delta G}{NkT_E}$ for the α-IMC, with a Jackson α factor of $\sim$3 [65, 66]. Fig.

8(a) also shows the plots for the β-IMC and Al as a comparison, with a Jackson factor of $\alpha \approx 4.5$ and $\alpha \approx 1.3$, respectively [65, 66].

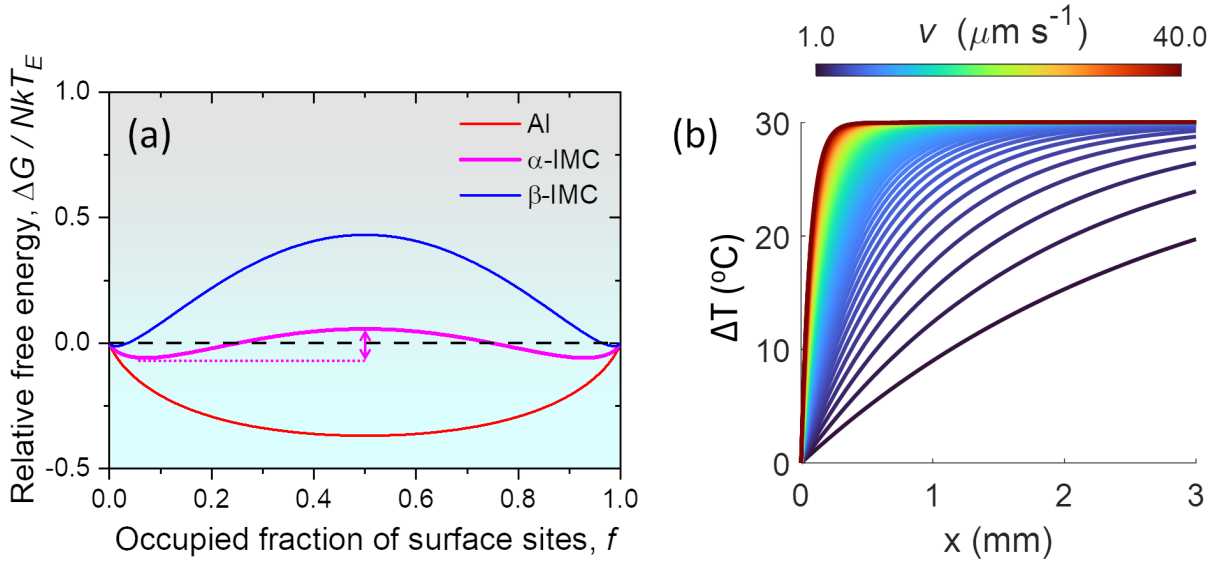

Figure 8: (a) Interface free energy as a function of occupied fraction of surface sites for α-IMC, Al and β-IMC, after Eq. 1. (b) The available undercooling ΔT in the liquid ahead of a growing IMC/liquid interface as a function of distance x, for interface velocities between 1 µm s^{-1} and 40 µm s^{-1}. The following parameters were used for the calculation of (b): $\Delta C_0 = -1$ wt%, $m = 30$ K wt.%$^{-1}$, $D_l = 3 \times 10^{-9}$ m^{2}s^{-1}.

For $\alpha < 2$ (e.g. Al), the minimum free energy is obtained when 50% of N sites are filled with atoms, i.e. the surface is atomically rough with a large number of sites available for atom attachment. Microscopically, these crystals therefore tend to grow with non-faceted morphologies. In comparison, for $\alpha > 2$ (e.g. β-IMC), two minima are obtained when the sites are nearly full or nearly empty, i.e. the surface is atomically flat with few sites available for atom attachment. Microscopically, such crystals tend to grow with faceted morphologies, controlled by crystallography. For α factors only slightly larger than 2 (e.g. α-IMC), crystal surfaces that are originally atomically flat under equilibrium conditions may become atomically rough (associated with increased randomness in surface atom attachment) at increased undercooling, which provides the additional energy for this metastable arrangement (indicated by a magenta double-headed arrow in the α-IMC curve in Fig. 8(a)). Under isothermal cooling conditions as in the experiments, the magnitude of the available undercooling ΔT in the liquid (also termed "constitutional supercooling" [67]), arising from the micro-segregation (depletion in this

case) of Fe in front of a growing Fe-rich IMC/liquid interface, is given by [44, 46]:

$$\Delta T(x, v) = m\Delta C_0(e^{-x\frac{v}{D_l}} - 1) \tag{2}$$

where m is the slope of the liquidus of equilibrium Al-Fe phase diagram in the region of interest, ΔC_0 is the composition difference between the bulk liquid and the liquid at the IMC/liquid interface, D_l is the Fe diffusion coefficient in the liquid, v is the growth velocity of the interface, and x is the distance from the interface. Fig. 8(b) presents a schematic depiction of the available undercooling from Eq. 2 as a function of the distance x under isothermal cooling, for different values of interface velocity from $1\,\mu m\,s^{-1}$ to $40\,\mu m\,s^{-1}$.

Table 4 lists the available undercooling ΔT in the vicinity of a growing IMC/liquid interface at different measured velocities, extracted from Fig. 8(b). At an interface velocity $v = 1.2\ \mu m\,s^{-1}$ (the median velocity for the α-IMC in Fig. 6), $\Delta T = 1\,°C$ at $100\,\mu m$ from the interface. At $v = 8\ \mu m\,s^{-1}$ (the median velocity for the α-IMC in Fig. 4), $\Delta T = 9\,°C$. Further increase to $40\,\mu m\,s^{-1}$ (the peak velocity for the α-IMC in Fig. 4) give $\Delta T = 23\,°C$ at the same distance from the interface. The higher the available undercooling adjacent to the IMC/liquid interface, resulting from increased interface velocity (solidification velocity), then the greater the interfacial metastability and tendency for roughening of the α-IMC crystal surface. Thus it is the solute undercooling at high growth rates that facilitates a transition from faceted polyhedral to non-faceted dendritic morphology.

Table 4: A list of available undercooling ΔT as a function of distance x from the IMC/liquid interface and interface velocity v, extracted from Fig. 8(b).

Velocity ($\mu m\,s^{-1}$)	**Distance** x (mm)			
	0.1	0.3	0.5	1
1.2	1 °C	3 °C	5 °C	9 °C
8	9 °C	20 °C	25 °C	29 °C
40	23 °C	30 °C	30 °C	30 °C

4.2 IMC start temperatures and phase selection

Following the procedure described in section 2.4, Figs. 9(a) and (b) show the formation start temperatures for the primary IMCs in 1.2Fe (Fig. 9(a)) and 2.5Fe (Fig. 9(b)) alloys. Consistent with the qualitative observations in Figs. 2 and 3, alloy 1.2Fe formed α-IMC as the only primary IMC across all cooling rates, and alloy 2.5Fe formed only primary α-IMC at $0.5\,\mathrm{K\,s^{-1}}$ and primary α-IMC with subsequent primary β-IMC at increased cooling rates. In both 1.2Fe and 2.5Fe alloys, the α-IMC start temperatures remained approximately constant regardless of cooling rate, showing a maximum undercooling of 3 °C. This indicates a relatively low nucleation barrier for α-IMC (noting the formation on unavoidable surface oxides previously described). In contrast, the formation of the more anisotropic (monoclinic structure) primary β-IMCs, in the 2.5Fe alloy, had a strong dependence on cooling rate, with a formation start temperature of 605±5 °C at $2\,\mathrm{K\,s^{-1}}$, which increased to 622±1 °C at $4\,\mathrm{K\,s^{-1}}$ and then 626±1 °C at $8\,\mathrm{K\,s^{-1}}$. These temperatures corresponded to 29 °C, 12 °C and 8 °C below the equilibrium β-IMC start temperature, respectively. Similarly, previous work by Feng *et al.* [44] on low-symmetry, monoclinic $Al_{13}Fe_4$ also revealed the same trend: a large formation undercooling of >20 °C at $1\,\mathrm{K\,s^{-1}}$ that gradually decreased with increasing cooling rate.

It is worth noting that the IMC formation undercooling is different from the available undercooling in the liquid. Whilst the available undercooling increases with cooling rate (Fig. 8(b)), the IMC formation undercooling (i.e. the undercooling required) depends on the nucleation barrier of the IMC and the potency of nucleants within the undercooled liquid volume. As described in more detail in section 4.3, an increased cooling rate promoted a larger volume fraction of liquid undercooled. For β-IMC that has a larger nucleation barrier than the α-IMC due to its larger entropy of fusion (Fig. 8(a)), nucleation tends to occur preferentially only on the more potent nucleants, which are however relatively rare. Increasing the cooling rate increased the solute undercooled liquid volume, therefore increased the chance that more potent nucleants were activated, and hence the mean formation undercooling reduced (Fig. 9(b)). This shows that when some solid has

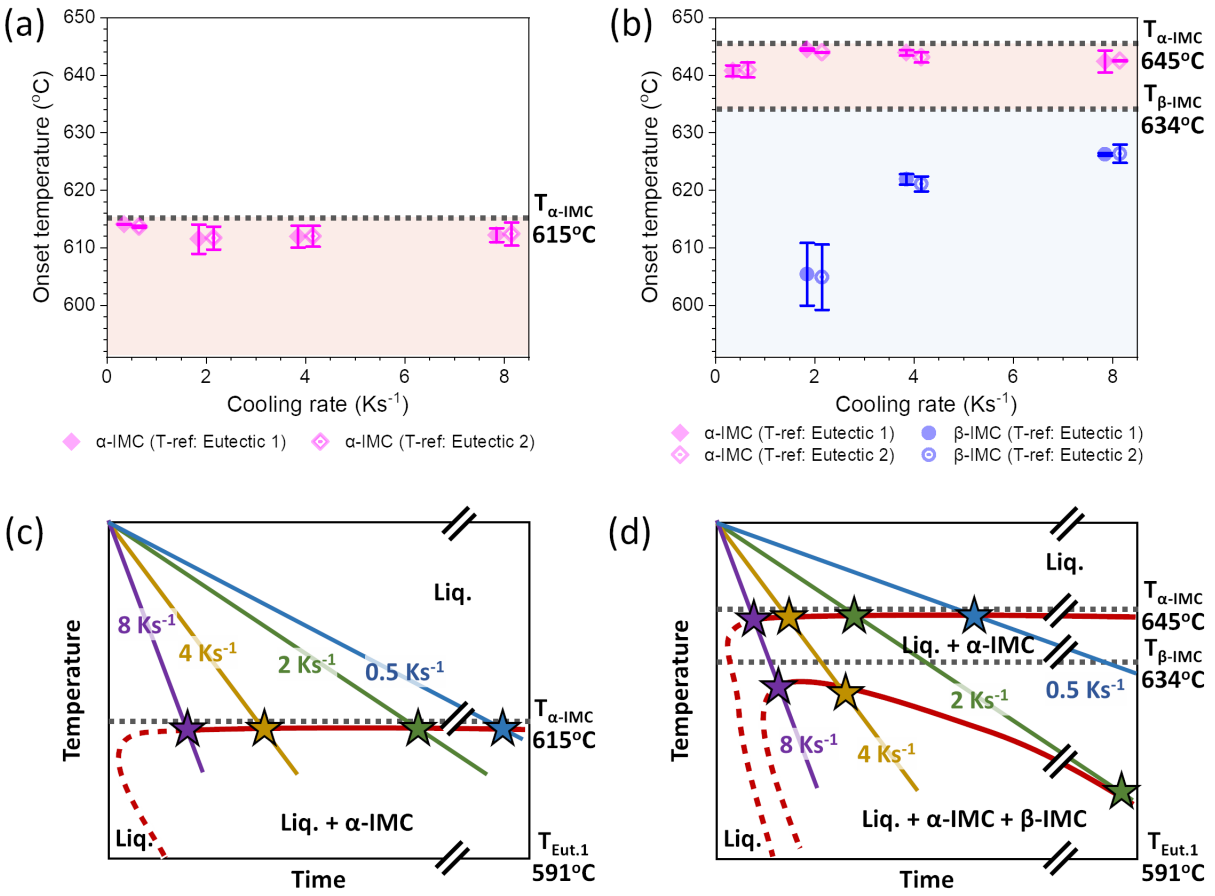

Figure 9: (a and b) Formation start temperatures of primary IMCs estimated from *in situ* radiographic data for (a) alloy 1.2Fe, and (b) alloy 2.5Fe. For each cooling condition, two eutectics were employed as independent temperature references for temperature estimation. (c and d) Schematic continuous cooling transformation (CCT) diagrams established based on (a and b) for (c) alloy 1.2Fe, and (d) alloy 2.5Fe.

already formed, as is the case here, it is critical to consider thermal-solute joint effects in the liquid, and not to consider isolated grain nucleation behaviour where only heat flow effects on undercooling are relevant.

To consolidate these findings and to more clearly illustrate IMC phase selection as a function of cooling condition, a schematic continuous cooling transformation (CCT) diagram was constructed for 1.2Fe (Fig. 9(c)) and 2.5Fe (Fig. 9(d)) respectively, based on the experimental datasets in Figs. 9(a) and (b). In each diagram, the coloured straight lines indicate cooling at constant rates from $0.5\,\mathrm{K\,s^{-1}}$ to $8\,\mathrm{K\,s^{-1}}$, and the star in the same colour indicates the measured IMC formation start temperature at each cooling rate, from which the CCT schematic diagrams were extrapolated. For alloy 1.2Fe (Fig. 9(c)), although cooling conditions did not affect primary IMC phase selection, a higher cooling

rate resulted in effective refinement of the primary α-IMCs (Fig. 2). For alloy 2.5Fe (Fig. 9(d)), recalling the enhanced formation of β-IMCs as the cooling rate increased from $2\,\mathrm{K\,s^{-1}}$ to $8\,\mathrm{K\,s^{-1}}$ (Fig. 3) and further to $\sim$100 $\mathrm{K\,s^{-1}}$ (Fig. S4 in the SM), it is suggested that to avoid the formation of the more mechanically deleterious, plate-like β-IMCs in very high Fe-containing recycled alloys (such as the 2.5Fe alloy), a relatively low cooling rate of just below $2\,\mathrm{K\,s^{-1}}$ should be used.

4.3 Solute suppression driven IMC phase selection

Section 4.1 focused on the solute diffusion field, the resulting undercooling generated in front of an individual IMC/liquid interface, and its effect on individual IMC morphology. In this section, the mechanism of IMC phase selection evolving with cooling rate in the higher Fe-containing 2.5Fe alloy is explored further, by considering the way in which Fe concentration in the liquid was distributed across the entire field of view. In particular, we consider the critical competition between the growth of pre-formed higher-temperature α-IMCs or instead, the additional nucleation and growth of lower-temperature β-IMCs. Consistent with the well-known interdependence model proposed by StJohn *et al.* [67], we now consider an ensemble of IMC crystals in the liquid. While thermal/solute equilibrium may hold at individual IMC/liquid interfaces (especially in the earlier solidification stage), the entire field of view is evidently in a non-equilibrium state since there are easily resolvable and profound Fe concentration gradient in the liquid. This arises as the Fe-rich IMCs grow and absorb Fe from the nearby liquid faster than diffusion can flatten the resulting Fe gradient.

Although the 2.5Fe alloy studied here is a multi-element alloy, X-ray absorption by Al, Si and Mg at the experimental X-ray beam energy (pink beam peaking at 25 keV) is negligible compared with Fe or Mn [68]. Further, the total Fe concentration in the liquid was $>$ 6 times larger than Mn, and the CALPHAD (CALculation of PHAse Diagram) simulations in Fig. S2 in the SM show that Fe and Mn segregate in the same trend during solidification. Therefore, it can be assumed that the X-ray absorption contrast in the

liquid is dominated by the differences in the local Fe concentration.

Following the procedure of image processing detailed in section S2 in the SM, false colour maps in Fig. 10 show the area fraction of Fe-depleted liquid (f_{L-dep}) during isothermal solidification at cooling rates from $0.5\,\mathrm{K\,s^{-1}}$ to $8\,\mathrm{K\,s^{-1}}$, for a temperature 8 °C below the equilibrium β-IMC formation start temperature. This is the temperature when β-IMC first appeared in the current work. Any Fe-depletion above this temperature was solely due to the formation and growth of the higher-temperature primary α-IMCs. The alloy solidified at $0.5\,\mathrm{K\,s^{-1}}$ had the largest area fraction of depleted liquid ($f_{L-dep} = 0.89$), which decreased with increasing cooling rate to 0.71 at $2\,\mathrm{K\,s^{-1}}$, 0.58 at $4\,\mathrm{K\,s^{-1}}$, and 0.39 at $8\,\mathrm{K\,s^{-1}}$. Similar observations of a shrinking solute affected zone with cooling rate were reported for equiaxed α-Al dendrites by Jia *et al.* at cooling rates up to 1 $\mathrm{Ks^{-1}}$ [69]; and more recently by Feng *et al.* for primary Pt-rich IMC crystals at cooling rates up to $8\,\mathrm{K\,s^{-1}}$ [46]. The effect of the Fe-depleted liquid is to reduce the effective undercooling experienced by the liquid, making nucleation of a new phase from the liquid less likely. The greater the magnitude of "solute suppression", and the greater the volume of liquid depleted, the more difficult it becomes for even potentially potent nucleants to catalyse crystal formation [46, 70].

Recalling that the IMCs formed on intrinsic oxides and remained static, Fig. 10(a) shows that at the lowest cooling rate of $0.5\,\mathrm{K\,s^{-1}}$, most of the liquid was solute depleted due to substantial growth of the relatively low number but relatively large α-IMCs. Therefore, many of the potential oxide nucleants that might otherwise be available to catalyse β-IMC nucleation were solute suppressed, evidenced by the lack of β-IMC formation even though the liquid was undercooled by 8 °C below the equilibrium β-IMC start temperature. In contrast, at faster cooling of $8\,\mathrm{K\,s^{-1}}$, there was little time for the growth of the larger number of pre-formed α-IMCs, leading to a smaller depleted liquid fraction. Now, there was a higher probability of potential oxide nucleants being active in the non-depleted liquid regions, and there was therefore more subsequent β-IMC formation. In other words, the probability of β-IMC nucleation depended on the time available for the growth of the

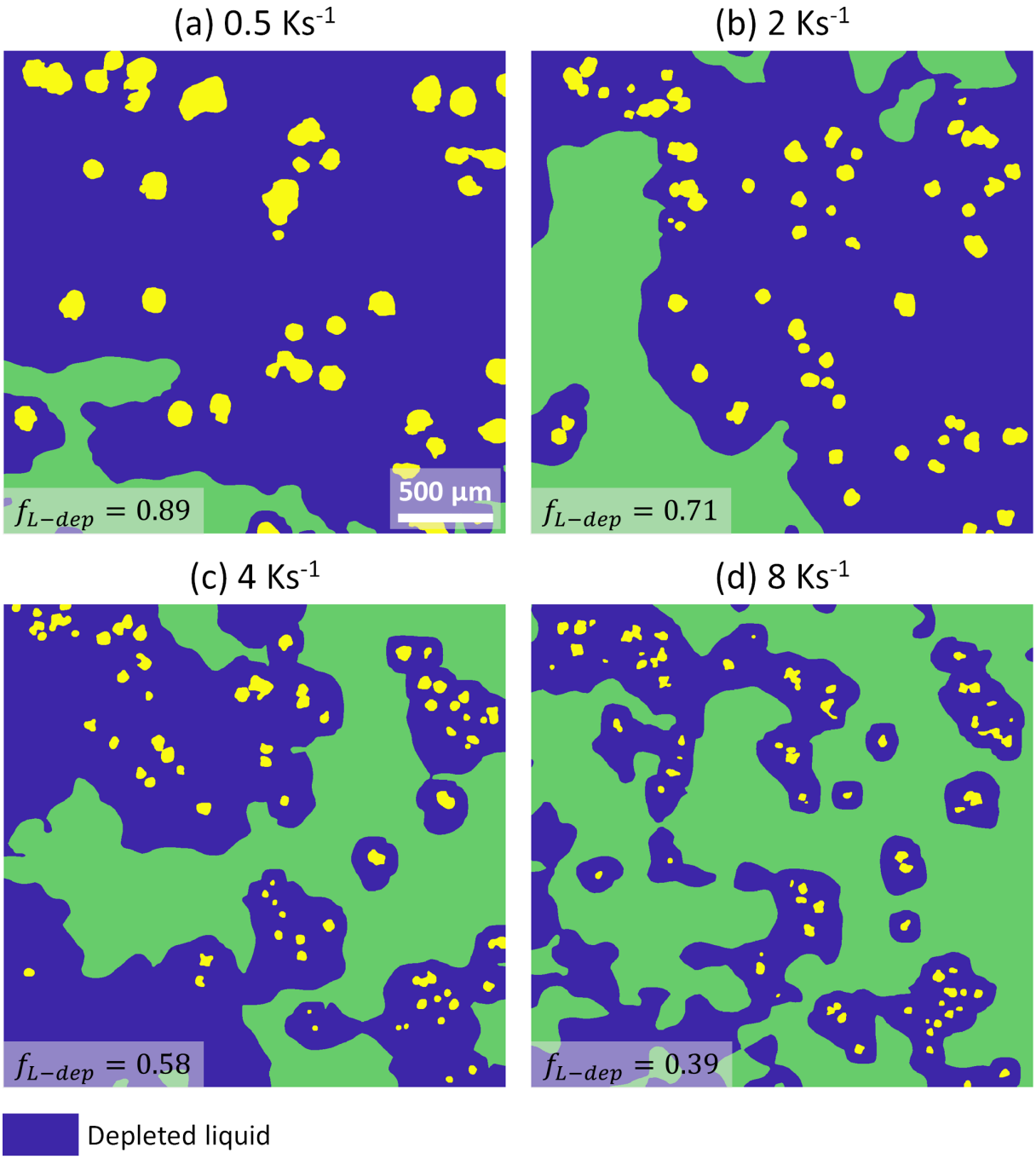

Figure 10: False colour maps showing the area fraction of Fe-depleted liquid (f_{L-dep}) at the temperature 8 °C below the equilibrium β-IMC start temperature during isothermal solidification at (a) 0.5 K s^{-1}, (b) 2 K s^{-1}, (c) 4 K s^{-1} and (d) 8 K s^{-1}. As described in section S2 in the SM, each image was obtained by subtracting the current frame with a reference frame of a flat intensity field acquired before solidification started. The Fe-depleted liquid was defined as pixels in the liquid where the greyscale intensity change $\Delta I > \Delta I^* = 0.03$, and is coloured blue in each image. The non-depleted liquid is coloured green, and the pre-formed α-IMCs are coloured yellow.

higher-temperature α-IMCs and the associated fraction of liquid solute depleted, both of which depended on the cooling rate.

One possibility that arises from these insights is that for high-Fe recycled alloys, a relative slow cooling rate of just below $\sim 2\,\mathrm{K\,s^{-1}}$ (e.g. controlled furnace cooling) could first be applied to promote the formation of comparatively benign non-faceted, near-equiaxed α-IMC dendrites. As described above, this would deplete the Fe concentration in the liquid and suppress the formation of the lower-temperature, more deleterious β-IMCs. Second, once these solute fields were established, it should then be possible to increase the cooling rate (e.g. by casting to shape), without realising a large population of coarse β-IMCs that would otherwise form. Our future work will explore variants of this two-step casting approach, and the resulting different populations of IMCs and their effect on macro-properties.

5 Conclusions

To inform process design strategies for recycling highly Fe-contaminated Al alloys, we investigated systematically the phase selection and morphological evolution of Fe-rich intermetallic compounds (IMCs) during the solidification of recycled 3xx series Al alloys with elevated Fe concentrations of 1.2 wt.% and 2.5 wt.%. Using *in situ* synchrotron X-ray radiography, novel insights into the kinetics and mechanisms of the critical α-AlFeSi (α-IMC)/β-AlFeSi (β-IMC) phase selection and α-IMC morphological evolution were unveiled over a cooling rate range of $0.5\,\mathrm{K\,s^{-1}}$ to $8\,\mathrm{K\,s^{-1}}$, complemented with post-solidification electron microscopy. The key findings were:

1. By integrating *in situ* synchrotron X-ray radiography with thermodynamic simulations, we developed a method to reliably estimate the formation start temperatures of individual Fe-rich IMC phases, allowing the kinetics of complex phase selections to be revealed under varied cooling conditions.

2. A 1.2Fe alloy formed α-IMCs as the only primary IMC, and as cooling rate increased from $0.5\,\mathrm{K\,s^{-1}}$ to $8\,\mathrm{K\,s^{-1}}$, there was a four-fold α-IMC size reduction from 82±18µm to 21±9µm.

3. Contrary to the widely held assumption that increasing cooling rates suppresses the formation of β-IMCs, in a more concentrated 2.5Fe alloy - where primary β-IMCs should form following primary α-IMCs under equilibrium conditions - lower cooling rates of $0.5\,\mathrm{K\,s^{-1}}$ fully suppressed the formation of primary β-IMCs, whilst increasing cooling rates significantly promoted the formation of primary β-IMCs. This trend was confirmed further in a water-cooled casting at a higher cooling rate of $\sim 100\,\mathrm{K\,s^{-1}}$.

4. A solute suppression-driven phase selection mechanism was proposed, by considering Fe depletion resulting from an ensemble of pre-formed α-IMCs. For the same temperature (below the equilibrium β-IMC start temperature), the lowest cooling rate led to most of the liquid being Fe-depleted, preventing the nucleation of lower-temperature β-IMCs; and in contrast higher cooling rate led to smaller fraction of depleted liquid, i.e. increased probability of high undercoolings been achieved and β-IMC nucleation. It was suggested that the probability of β-IMC nucleation was therefore dependent on the time available for the growth of pre-existing α-IMCs and the associated fraction of Fe depleted liquid, both of which dictated by the cooling rate.

5. There was a faceted-to-non-faceted transition in α-IMC morphology in the 2.5Fe alloy. The morphological transition from a polyhedron to a near-equiaxed dendrite was attributed to increased liquid undercooling ahead of the IMC/liquid interface at increased solidification velocity: at a distance 100 µm ahead of the IMC/liquid interface, the liquid undercooling increased from 1 °C to 23 °C as the solidification velocity increased from $1.2\,\mathrm{\mu m\,s^{-1}}$ to $40\,\mathrm{\mu m\,s^{-1}}$. These undercoolings provided sufficient metastability of the solid/liquid interface such that the energy barrier of a faceted-to-non-faceted transition was overcome.

6. A more benign (dendritic α-rich, β-deficient) microstructure may be achieved, even in a highly contaminated 2.5Fe alloy, by casting at an intermediate cooling rate just

below $\sim$2 K s^{-1}, which promotes the nucleation of more isotropic, dendritic primary α-IMCs and suppresses the subsequent formation of more deleterious primary β-IMCs.

Together, these findings provide new insights into the complex interplay between composition, solidification conditions, IMC species and interfacial morphologies in recycled Al alloys. They contribute to a growing understanding that may inform the design of processing strategies for more benign IMC types and morphologies in recycled alloys.

Declaration of Competing Interest

The authors declare that they have no known competing financial interests or personal relationships that could have appeared to influence the work reported in this paper.

Declaration of Generative AI and AI-assisted technologies in the writing process

During the early preparation of this work the author(s) used Chat GPT in order to improve readability. After using this tool/service, the author(s) reviewed and edited the content as needed and take full responsibility for the content of the publication.

Acknowledgements

This work was supported by EPSRC (UK) under grant numbers EP/W024829/1 (Live X-Ray imaging) and EP/X03884X/1 (Artificial Intelligence X-ray Imaging for Sustainable Metal Manufacturing). We gratefully acknowledge Diamond Light Source for beamtime at I13-2, under proposal No. MG36212; Principal Advisor Francis Breton and R&D Manager Melanie Saucier at Rio Tinto for in-kind support of raw materials and time for discussion.

Data availability

Data will be made available on request.

References

[1] J. A. Taylor, Iron-Containing Intermetallic Phases in Al-Si Based Casting Alloys, Procedia Mater. Sci. 1 (2012) 19–33.

[2] K. Robinson, P. J. Black, An X-Ray examination of an α (Al-Fe-Si) ternary compound, London, Edinburgh, Dublin Philos. Mag. J. Sci. 44 (359) (1953) 1392–1397.

[3] M. Cooper, The crystal structure of the ternary alloy α(AlFeSi), Acta Crystallogr. 23 (6) (1967) 1106–1107.

[4] C. Y. Sun, L. F. Mondolfo, A clarification of phases occurring in aluminium-rich aluminium-iron-silicon alloys, J. Inst. Met. 95 (1967) 384.

[5] C. M. Adam, L. M. Hogan, Crystallography of the Al-Al3 Fe eutectic, Acta Metall. 23 (3) (1975) 345–354.

[6] V. Stefaniay, A. Griger, T. Turmezey, Intermetallic phases in the aluminium-side corner of the AlFeSi-alloy system, J. Mater. Sci. 22 (2) (1987) 539–546.

[7] J. Grin, U. Burkhardt, M. Ellner, K. Peters, Refinement of the Fe4Al13 structure and its relationship to the quasihomological homeotypical structures, Zeitschrift fuer Krist. 209 (6) (1994) 479–487.

[8] A. Griger, V. Stefaniay, Equilibrium and non-equilibrium intermetallic phases in Al-Fe and Al-Fe-Si alloys, J. Mater. Sci. 31 (24) (1996) 6645–6652.

[9] C. M. Allen, K. A. Q. O'Reilly, B. Cantor, P. V. Evans, Intermetallic phase selection in 1XXX Al alloys, Prog. Mater. Sci. 43 (2) (1998) 89–170.

[10] Z.-K. Liu, Y. A. Chang, Thermodynamic assessment of the Al-Fe-Si system, Metall. Mater. Trans. A 30 (4) (1999) 1081–1095.

[11] X. Cao, J. Campbell, The nucleation of Fe-Rich phases on oxide films in Al-11.5Si-0.4Mg cast alloys, Metall. Mater. Trans. A 34 (7) (2003) 1409–1420.

[12] W. Khalifa, F. H. Samuel, J. E. Gruzleski, Iron intermetallic phases in the Al corner of the Al-Si-Fe system, Metall. Mater. Trans. A 34 (13) (2003) 807–825.

[13] S. G. Shabestari, The effect of iron and manganese on the formation of intermetallic compounds in aluminum–silicon alloys, Mater. Sci. Eng. A 383 (2) (2004) 289–298.

[14] G. Sha, K. O'Reilly, B. Cantor, Characterization of Fe-Rich Intermetallic Phases in a 6xxx Series Al Alloy, Mater. Sci. Forum 519-521 (2006) 1721–1726.

[15] K. Liu, X. Cao, X. Chen, A New Iron-Rich Intermetallic-Al m Fe Phase in Al-4.6Cu-0.5Fe Cast Alloy, Metall. Mater. Trans. A 43 (4) (2012) 1097–1101.

[16] K. Liu, X. Cao, X. Chen, Formation and Phase Selection of Iron-Rich Intermetallics in Al-4.6Cu-0.5Fe Cast Alloys, Metall. Mater. Trans. A 44 (2) (2012) 682–695.

[17] D. Raabe, D. Ponge, P. J. Uggowitzer, M. Roscher, M. Paolantonio, C. Liu, H. Antrekowitsch, E. Kozeschnik, D. Seidmann, B. Gault, F. De Geuser, A. Deschamps, C. Hutchinson, C. Liu, Z. Li, P. Prangnell, J. Robson, P. Shanthraj, S. Vakili, C. Sinclair, L. Bourgeois, S. Pogatscher, Making sustainable aluminum by recycling scrap: The science of "dirty" alloys, Prog. Mater. Sci. 128 (2022) 100947.

[18] D. Raabe, The Materials Science behind Sustainable Metals and Alloys, Chem. Rev. 123 (5) (2023) 2436–2608.

[19] S. Ji, W. Yang, F. Gao, D. Watson, Z. Fan, Effect of iron on the microstructure and mechanical property of Al–Mg–Si–Mn and Al–Mg–Si diecast alloys, Mater. Sci. Eng. A 564 (2013) 130–139.

[20] L. Ceschini, I. Boromei, A. Morri, S. Seifeddine, I. L. Svensson, Microstructure, tensile and fatigue properties of the Al-10%Si-2%Cu alloy with different Fe and Mn content cast under controlled conditions, J. Mater. Process. Technol. 209 (15-16) (2009) 5669–5679.

[21] L. F. Mondolfo, Aluminum alloys : structure and properties, Butterworths, 1976.

[22] J. E. Hatch, Aluminum properties and physical metallurgy, Metals Park, OH : American Society for Metals, 1984.

[23] C. M. Dinnis, J. A. Taylor, A. K. Dahle, Interactions between iron, manganese, and the Al-Si eutectic in hypoeutectic Al-Si alloys, Metall. Mater. Trans. A 37 (11) (2006) 3283–3291.

[24] S. Murali, K. S. Raman, K. S. S. Murthy, Morphological studies on β-FeSiAl5 phase in Al-7-Si-0.3Mg alloy with trace additions of Be, Mn, Cr, and Co, Mater. Charact. 33 (2) (1994) 99–112.

[25] P. Ashtari, H. Tezuka, T. Sato, Influence of Sr and Mn Additions on Intermetallic Compound Morphologies in Al-Si-Cu-Fe Cast Alloys, Mater. Trans. 44 (12) (2003) 2611–2616.

[26] H. Kim, T. Park, S. Han, H. Lee, Effects of Mn on the crystal structure of α-Al(Mn,Fe)Si particles in A356 alloys, J. Cryst. Growth 291 (1) (2006) 207–211.

[27] S. S. Sreeja-Kumari, R. M. Pillai, T. P. D. Rajan, B. C. Pai, Effects of individual and combined additions of Be, Mn, Ca and Sr on the solidification behaviour, structure and mechanical properties of Al–7Si–0.3Mg–0.8Fe alloy, Mater. Sci. Eng. A 460 (2007) 561–573.

[28] C. Tseng, S. Lee, S. Tsai, C. Cheng, Effects of manganese on microstructure and mechanical properties of A206 alloys containing iron, J. Mater. Res. 17 (09) (2002) 2243–2250.

[29] C. Bidmeshki, V. Abouei, H. Saghafian, S. Shabestari, M. Noghani, Effect of Mn addition on Fe-rich intermetallics morphology and dry sliding wear investigation of hypereutectic Al-17.5%Si alloys, J. Mater. Res. Technol. 5 (3) (2016) 250–258.

[30] S. K. Shaha, F. Czerwinski, W. Kasprzak, J. Friedman, D. L. Chen, Effect of Cr, Ti, V, and Zr Micro-additions on Microstructure and Mechanical Properties of the Al-Si-Cu-Mg Cast Alloy, Metall. Mater. Trans. A 47 (5) (2016) 2396–2409.

[31] M. Mahta, M. Emamy, A. Daman, A. Keyvani, J. Campbell, Precipitation of Fe rich intermetallics in Cr- and Co-modified A413 alloy, Int. J. Cast Met. Res. 18 (2) (2005) 73–79.

[32] S. Murali, S. Muthukkaruppan, K. S. Raman, K. S. S. Murthy, Stir cast and extruded Al-7Si-0.3Mg alloy containing iron and beryllium, Mater. Sci. Technol. 13 (4) (1997) 337–342.

[33] F. H. Samuel, A. M. Samuel, H. W. Doty, S. Valtierra, Influence of composition, Sr modification, and annealing treatment on the structure and properties of cast Al-4 pct Mg alloys, Metall. Mater. Trans. A 34 (1) (2003) 115–129.

[34] S. Yie, S.and Lee, Y. Lin, J. Lin, Mechanical Properties of Al-11%Si Casting Alloys Containing Trace Be and Sr, Mater. Trans. JIM 40 (4) (1999) 294–300.

[35] L. A. Narayanan, F. H. Samuel, J. E. Gruzleski, Crystallization behavior of iron-containing intermetallic compounds in 319 aluminum alloy, Metall. Mater. Trans. A 25 (8) (1994) 1761–1773.

[36] G. Sha, K. O'Reilly, B. Cantor, J. Worth, R. Hamerton, Growth related metastable phase selection in a 6xxx series wrought Al alloy, Mater. Sci. Eng. A 304-306 (2001) 612–616.

[37] S. Seifeddine, S. Johansson, I. L. Svensson, The influence of cooling rate and man-

ganese content on the β-Al5FeSi phase formation and mechanical properties of Al–Si-based alloys, Mater. Sci. Eng. A 490 (1-2) (2008) 385–390.

[38] M. J. Castro-Roman, I. Aguilera-Luna, A. A. Gaona-Coronado, M. Herrera-Trejo, J. Torres, Role of Fe/Mn Ratio and Cooling Rate on Precipitation of Iron Intermetallics α-AlFeMnSi and β-AlFeSi in a 356 Alloy, Trans. Indian Inst. Met. 68 (6) (2015) 1193–1197.

[39] Y. Zhao, D. Song, H. Wang, X. Li, L. Chen, Z. Sun, Z. Wang, T. Zhai, Y. Fu, Y. Wang, S. Liu, Y. Du, W. Zhang, Revealing the nucleation and growth mechanisms of Fe-rich phases in Al–Cu–Fe(-Si) alloys under the influence of Al–Ti–B, Intermetallics 146 (2022) 107584.

[40] Z. Que, Y. Wang, Z. Fan, T. Hashimoto, X. R. Zhou, Composition templating for heterogeneous nucleation of intermetallic compounds, Scientific Reports 14 (1) (2024) 1–19.

[41] Y. Xuan, T. Liu, L. Nastac, L. Brewer, I. Levin, V. Arvikar, The Influence of Ultrasonic Cavitation on the Formation of Fe-Rich Intermetallics in A383 Alloy, Metallurgical and Materials Transactions A 49 (8) (2018) 3346–3357.

[42] S. Feng, E. Liotti, A. Lui, S. Kumar, A. Mahadevegowda, K. A. Q. O'Reilly, P. S. Grant, An in-situ method to estimate the tip temperature and phase selection of secondary Fe-rich intermetallics using synchrotron X-ray radiography, Scr. Mater. 149 (2018) 44–48.

[43] S. Feng, Y. Cui, E. Liotti, A. Lui, C. Gourlay, P. Grant, In-situ X-ray radiography of twinned crystal growth of primary Al13Fe4, Scr. Mater. 184 (2020) 57–62.

[44] S. Feng, E. Liotti, A. Lui, M. D. Wilson, T. Connolley, R. H. Mathiesen, P. S. Grant, In-situ X-ray radiography of primary Fe-rich intermetallic compound formation, Acta Mater. 196 (2020) 759–769.

[45] Y. Zhao, W. Zhang, D. Song, B. Lin, F. Shen, D. Zheng, C. X. Xie, Z. Sun, Y. Fu, R. Li, Nucleation and growth of Fe-rich phases in Al-5Ti-1B modified Al-Fe alloys investigated using synchrotron X-ray imaging and electron microscopy, J. Mater. Sci. Technol. 80 (2021) 84–99.

[46] S. Feng, E. Liotti, A. Lui, M. D. Wilson, P. S. Grant, Nucleation bursts of primary intermetallic crystals in a liquid Al alloy studied using in situ synchrotron X-ray radiography, Acta Mater. 221 (2021) 117389.

[47] Z. Song, O. V. Magdysyuk, L. Tang, T. Sparks, B. Cai, Growth dynamics of faceted Al13Fe4 intermetallic revealed by high-speed synchrotron X-ray quantification, J. Alloys Compd. 861 (2021) 158604.

[48] S. Feng, Z. Jin, W. Du, I. Han, A. Lui, X. Zhou, P. R. Shearing, P. S. Grant, E. Liotti, The mechanism of Fe-rich intermetallic compound formation and growth on inoculants revealed by electron backscattered diffraction and X-ray imaging, Mater. Des. 232 (2023) 112110.

[49] K. Xiang, L. Qin, Y. Zhao, S. Huang, W. Du, E. Boller, A. Rack, M. Li, J. Mi, Operando study of the dynamic evolution of multiple Fe-rich intermetallics of an Al recycled alloy in solidification by synchrotron X-ray and machine learning, Acta Mater. 279 (2024) 120267.

[50] K. A. Jackson, Liquid metals and solidification, Asm, Cleveland 174 (1958).

[51] K. Jackson, D. Uhlmann, J. Hunt, On the nature of crystal growth from the melt, J. Cryst. Growth 1 (1) (1967) 1–36.

[52] ASTM International, Standard Practices for Sampling and Sample Preparation of Aluminum and Aluminum Alloys for Determination of Chemical Composition by Spark Atomic Emission Spectrometry (2021).

[53] S. Feng, E. Liotti, P. S. Grant, X-ray Imaging of Alloy Solidification: Crystal Formation, Growth, Instability and Defects, Materials (Basel). 15 (4) (2022) 1319.

[54] S. Feng, I. Han, A. Lui, R. Vincent, G. Ring, P. S. Grant, E. Liotti, Investigating Metal Solidification with X-ray Imaging, Metals (Basel). 12 (3) (2022) 395.

[55] G. Farnebäck, Two-frame motion estimation based on polynomial expansion, in: Image Analysis: 13th Scandinavian Conference, SCIA 2003 Halmstad, Sweden, June 29–July 2, 2003 Proceedings 13, Springer, 2003, pp. 363–370.

[56] T. Liu, M. Karkkainen, L. Nastac, V. Arvikar, I. Levin, L. N. Brewer, Iron-rich intermetallics in high pressure die cast A383 aluminum alloys, Intermetallics 126 (2020) 106814.

[57] A. Gorny, J. Manickaraj, Z. Cai, S. Shankar, Evolution of Fe based intermetallic phases in Al–Si hypoeutectic casting alloys: Influence of the Si and Fe concentrations, and solidification rate, J. Alloys Compd. 577 (2013) 103–124.

[58] Z. Ding, L. Yu, N. Zhang, W. Lu, J. Li, Q. Hu, Unveiling the growth and morphological transition mechanisms of Al2Cu intermetallic compounds quantified by synchrotron X-ray tomography, J. Mater. Sci. Technol. 209 (2025) 43–54.

[59] H. Kang, T. Wang, X. Li, Y. Su, J. Guo, H. Fu, Faceted-nonfaceted growth transition and 3-D morphological evolution of primary Al6Mn microcrystals in directionally solidified Al-3 at.% Mn alloy, J. Mater. Res. 29 (11) (2014) 1256–1263.

[60] J. Xian, S. Belyakov, M. Ollivier, K. Nogita, H. Yasuda, C. Gourlay, Cu6Sn5 crystal growth mechanisms during solidification of electronic interconnections, Acta Mater. 126 (2017) 540–551.

[61] M. Szurgot, J. Prywer, Growth Velocities and Disappearance of Faces of Crystals, Cryst. Res. Technol. 26 (2) (1991) 147–153.

[62] J. Prywer, Three-dimensional model of the disappearance of triangular faces in the crystal habit, J. Cryst. Growth 165 (3) (1996) 335–340.

[63] G. Wulff, Zur Frage der Geschwindigkeit des Wachsthums und der Auflösung der Krystallflächen, Zeitschrift für Krist. - Cryst. Mater. 34 (1901) 449–530.

[64] W. K. Burton, N. Cabrera, F. C. Frank, The growth of crystals and the equilibrium structure of their surfaces, Philos. Trans. R. Soc. London. Ser. A, Math. Phys. Sci. 243 (866) (1951) 299–358.

[65] M. Shakiba, N. Parson, X. G. Chen, Effect of homogenization treatment and silicon content on the microstructure and hot workability of dilute Al-Fe-Si alloys, Mater. Sci. Eng. A 619 (2014) 180–189.

[66] Q. Li, J. Wang, X. Liu, C. Xue, S. Wang, X. Yang, G. Tian, H. Su, X. Wu, Y. Miao, Accelerating the dissolution and transformation of detrimental Fe-rich intermetallics in recycled Al-Mg-Si alloy by homogenization and hot deformation, Mater. Charact. 213 (2024) 114024.

[67] D. H. Stjohn, M. Qian, M. A. Easton, P. Cao, The Interdependence Theory: The relationship between grain formation and nucleant selection, Acta Mater. 59 (12) (2011) 4907–4921.

[68] W. U. Mirihanage, K. V. Falch, I. Snigireva, A. Snigirev, Y. J. Li, L. Arnberg, R. H. Mathiesen, Retrieval of three-dimensional spatial information from fast in situ two-dimensional synchrotron radiography of solidification microstructure evolution, Acta Mater. 81 (2014) 241–247.

[69] Y. Jia, H. Huang, Y. Fu, G. Zhu, D. Shu, B. Sun, D. StJohn, An in situ investigation of the solute suppressed nucleation zone in an Al-15Cu alloy inoculated by Al-Ti-B, Scr. Mater. 167 (2019) 6–10.

[70] E. Liotti, C. Arteta, A. Zisserman, A. Lui, V. Lempitsky, P. S. Grant, Crystal nucleation in metallic alloys using x-ray radiography and machine learning, Sci. Adv. 4 (4) (2018) eaar4004.